Biochemical Pharmacology 82 (2011) 1604–1618

Contents lists available at SciVerse ScienceDirect

Biochemical Pharmacology

journal homepage: www.elsevier.com/locate/biochempharm

M2, a novel anthracenedione, elicits a potent DNA damage response that can be subverted through checkpoint kinase inhibition to generate mitotic catastrophe

Benny J. Evison [a], Mile Pastuovic [a], Rebecca A. Bilardi [a], Robert A. Forrest [a], Paul P. Pumuye [a], Brad E. Sleebs [b], Keith G. Watson [b], Don R. Phillips [a], Suzanne M. Cutts [a,*]

[a] Department of Biochemistry, La Trobe University, Victoria 3086, Australia
[b] The Walter and Eliza Hall Institute of Medical Research, Parkville, Victoria 3052, Australia

ARTICLE INFO

Article history:
Received 23 June 2011
Accepted 11 August 2011
Available online 30 August 2011

Keywords:
Topoisomerase II
Anthracenedione
Double strand break
Checkpoint kinase
Mitotic catastrophe

ABSTRACT

Pixantrone is a promising anti-cancer aza-anthracenedione that has prompted the development of new anthracenediones incorporating symmetrical side-chains of increasing length varying from two to five methylene units in each pair of drug side-chains. A striking relationship has emerged in which anthracenedione-induced growth inhibition and apoptosis was inversely associated with side-chain length, a relationship that was attributable to a differential ability to stabilise the topoisomerase II (TOP2) cleavage complex. Processing of the complex to a DNA double strand break (DSB) flanked by γH2AX in nuclear foci is likely to occur, as the generation of the primary lesion was antecedent to γH2AX induction. M2, bearing the shortest pair of side-chains, induced TOP2-mediated DSBs efficiently and activated cell cycle checkpoints via Chk1 and Chk2 phosphorylation, implicating the involvement of ATM and ATR, and induced a protracted S phase and subsequent G2/M arrest. The inactive analogue M5, containing the longest pair of side-chains, only weakly stimulated any of these responses, suggesting that efficient stabilisation of the TOP2 cleavage complex was crucial for eliciting a strong DNA damage response (DDR). An M2 induced DDR in p53-defective MDA-MB-231 cells was abrogated by UCN-01, a ubiquitous inhibitor of kinases including Chk1, in a response associated with substantial mitotic catastrophe and strong synergy. The rational selection of checkpoint kinase inhibitors may significantly enhance the therapeutic benefit of anthracenediones that efficiently stabilise the TOP2 cleavage complex.

1. Introduction

Pixantrone (Table 1) is a novel 2-aza-anthracenedione originally developed to improve the clinical profile of mitoxantrone (Table 1), a 5,8-dihydroxy analogue of pixantrone frequently applied in the treatment of lymphomas, leukaemias, advanced (metastatic) breast cancer and, more recently, prostate cancer [1,2]. Although mitoxantrone is clinically well tolerated, it still exerts a range of toxic side-effects including cardiotoxicity [3]. The development of pixantrone, currently in Phase III trials for the treatment of aggressive non-Hodgkins lymphoma [4], represents an effort to minimise the cardiotoxicity induced by mitoxantrone without compromising its therapeutic profile.

The mechanism of action of the anthracenediones is likely to be multimodal. Both mitoxantrone and pixantrone interact with DNA via intercalation *in vitro*, an event widely considered as critical to their mechanism(s) of action [5,6]. At a cellular level, localisation studies have established that mitoxantrone targets DNA and RNA of the nucleus [7,8], where it potently inhibits nucleic acid synthesis [9].

Topoisomerase II (TOP2), a nuclear enzyme responsible for regulating DNA topology by introducing transient breaks in both DNA strands, is a well established molecular target of the anthracenediones. Both mitoxantrone and pixantrone can function as TOP2 poisons by trapping and stabilising the normally transiently bound protein–DNA complex [6,10–12], thereby giving rise to DNA double strand breaks (DSBs). Despite their ability to stimulate DNA scission via TOP2, the potency of these anthracenediones as cytotoxic compounds does not always directly

Abbreviations: AN-9, pivaloyloxymethyl butyrate; ATM, ataxia telangiectasia mutated; ATR, ataxia telangiectasia mutated-related; CC, closed; Chk1, checkpoint kinase 1; Chk2, checkpoint kinase 2; CI, combination index; DDR, DNA damage response; DNA-PK, DNA protein kinase; DSB, double strand break; γH2AX, phosphorylated H2AX; IC_{50}, 50% inhibitory concentration; K_{app}, apparent binding constant; kDNA, kinetoplast DNA; MTT, 3-(4,5-dimethyl-2-thiazolyl)-2,5-diphenyl-2H-tetrazolium bromide; MX, mitoxantrone; NAC, N-acetyl-cysteine; NC, decatenated nicked; OTM, olive tail moment; PIX, pixantrone; PMSF, phenylmethylsulfonyl fluoride; ROS, reactive oxygen species; Sur, suramin; TOP2, topoisomerase II.

* Corresponding author. Tel.: +61 39 479 1517; fax: +61 39 479 1266.
E-mail addresses: b.evison@latrobe.edu.au (B.J. Evison), M.Pastuovic@latrobe.edu.au (M. Pastuovic), R.Bilardi@latrobe.edu.au (R.A. Bilardi), R.Forrest@latrobe.edu.au (R.A. Forrest), P.Pumuye@latrobe.edu.au (P.P. Pumuye), sleebs@wehi.edu.au (B.E. Sleebs), kwatson@wehi.edu.au (K.G. Watson), D.Phillips@latrobe.edu.au (D.R. Phillips), S.Cutts@latrobe.edu.au (S.M. Cutts).

0006-2952/$ – see front matter © 2011 Elsevier Inc. All rights reserved.
doi:10.1016/j.bcp.2011.08.013

Table 1
The generic chemical structure and R groups of each anthracenedione. K_{app} values represent the mean apparent equilibrium binding constant ± SEM of three independent experiments. TOP2 IC_{50} values indicate the concentration of each anthracenedione required for 50% inhibition of TOP2 decatenation activity as depicted in Fig. 4C. Growth inhibitory IC_{50} values indicate the concentration of each anthracenedione (nM) required to inhibit the growth of the specified cancer cells by 50% as evaluated using an MTT assay. Each value represents the IC_{50} mean ± SEM of *n* independent experiments, where *n* is indicated in parentheses alongside.

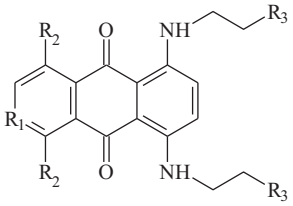

.

Compound	R_1	R_2	R_3	$K_{app} \times 10^{-7}$ (M^{-1})	TOP2 IC_{50} (μM)	Growth inhibition IC_{50} (nM)		
						HL-60[a]	A2780	PC-3
M2	CH	OH	NH_2	8.76 ± 0.43	1.3	9.3 ± 2.3 (2)	36 ± 4.5 (2)	280 ± 40 (2)
M3			CH_2NH_2	9.54 ± 0.31	1.4	260 ± 64 (3)	140 ± 24 (3)	2800 ± 520 (3)
M4			$(CH_2)_2NH_2$	10.2 ± 0.16	3.2	1800 ± 130 (3)	1600 ± 300 (3)	4700 ± 860 (3)
M5			$(CH_2)_3NH_2$	8.43 ± 0.53	5.6	3800 ± 630 (3)	7600 ± 1400 (3)	11,000 ± 2500 (3)
Mitoxantrone			$NH(CH_2)_2OH$	9.10 ± 0.46	ND	6.5 ± 1.5 (2)	29 ± 28 (2)	290 ± 38 (3)
Pixantrone	N	H	NH_2	ND	ND	400 ± 68 (4)	23 ± 4.5 (4)	1800 ± 650 (3)

[a] Indicates data that has previously been published by Mansour et al. [20].

correlate with their induction of DNA strand breaks [6,10,13,14], indicating that they may also be operating by a distinct, currently undefined mechanism of cell kill.

A novel form of anthracenedione–DNA interaction has emerged in which both mitoxantrone and pixantrone can be activated by formaldehyde to yield covalent drug–DNA adducts [15,16]. Mitoxantrone was the original anthracenedione to be identified that was susceptible to formaldehyde-mediated DNA alkylation [15], however mitoxantrone–DNA adducts are typically intrinsically unstable and require very high, biologically irrelevant drug concentrations for their formation [17]. A subsequent study established that, relative to mitoxantrone, pixantrone was clearly more efficient in its alkylation of DNA following formaldehyde activation, most likely by virtue of its terminal primary amino groups in each side-chain [16]. In cellular systems, pixantrone exhibits a mild synergistic relationship with the formaldehyde-releasing prodrug AN-9, indicating a favourable role for formaldehyde in mediating pixantrone-induced cell kill (unpublished observations).

A variety of methods including *in vitro* transcription and mass spectrometry have established that formaldehyde-activated pixantrone is a monofunctional DNA alkylator that binds selectively to CpG and CpA dinucleotides via the exocyclic N2 amino group of guanine within DNA [18]. Crucially, formaldehyde provides the methylene bridge that extends from the guanine residue and connects with a single amino group in one drug side-chain, thereby generating an aminal linkage [18]. Mitoxantrone forms an analogous formaldehyde-mediated DNA lesion [19], however its aminal functional group is much less stable [16], most likely because the secondary amino group is involved rather than the primary amine function of pixantrone.

A major functional limitation of both mitoxantrone– and pixantrone–DNA monoadducts is their relatively poor intrinsic stability (about 25 and 80 min, respectively [16]). It was subsequently rationalised that an increase in drug side-chain length may permit the anthracenedione to completely bridge the two strands of duplex DNA [18,20], much like an interstrand crosslink. The most potent and effective alkylating agents applied in cancer therapy are typically those that covalently crosslink the complementary strands of DNA, rather than alkylation of just one [21].

Accordingly, new anthracenediones were synthesised that incorporated extended aliphatic symmetrical side-chains, each terminating in a primary amino group critical for efficient activation by formaldehyde ([20] and Table 1). Importantly, these compounds retained the polycyclic anthraquinone ring system necessary for an intercalative interaction with DNA [22]. An *in vitro* crosslinking assay demonstrated that side-chain extension generally conferred a remarkable increase in the temporal stability of formaldehyde-activated anthracenedione–DNA adducts [20]. A clear and direct relationship existed between side-chain length and drug–DNA adduct half-life, with M5 (Table 1) exhibiting the most exceptional stability ($t_{1/2} > 2$ days). Significantly, the enhanced drug–DNA adduct stability was reflected in a range of cultured cancer cell lines where anthracenediones with longer side-chains (Table 1) were synergistic in combination with the formaldehyde-releasing prodrug AN-9 [20].

A further distinctive feature of the study [20] was that, as single agents, drug-induced growth inhibition was inversely but tightly associated with compound side-chain length. Moreover, the compound possessing the shortest pair of side-chains, M2 (Table 1), demonstrated exceptional growth inhibitory properties in cultured cancer cells comparable to the parent mitoxantrone [20]. Although many of these anthracenediones were originally synthesised and described more than 30 years ago [23–25], little effort has been made to characterise the underlying molecular mechanism(s) responsible for this variation in biological activity. Throughout the same period, tremendous advancements have been made in identifying the molecular alterations responsible for cancer development [26], and it is now clear that most, if not all, cancers harbour a compromised DDR system [26–28], a property that distinguishes them from cells of healthy tissue. Cancer-specific impairments in DDR systems may enable the selective targeting of cancers exposed to DNA damaging agents. Thirty years on, it is timely to exploit these recent advances by better characterising the molecular mechanisms(s) underlying the variation in anthracenedione-induced cell kill [20], the primary focus of the present study.

2. Methods

2.1. Materials

Mitoxantrone dihydrochloride, suramin, UCN-01, propidium iodide, Hoechst 33258, N-acetyl-L-cysteine, aprotinin, phenylmethylsulfonyl fluoride (PMSF), RNase A, rabbit α-actin antibody,

paraformaldehyde, Triton X-100, nonidet P-40, poly-L-lysine solution (0.1% w/v), 3-(4,5-dimethyl-2-thiazolyl)-2,5-diphenyl-2H-tetrazolium bromide (MTT) and low gelling temperature agarose (Type VII) were purchased from Sigma Chemical Co. (St. Louis, MO). Pixantrone was provided by Cell Therapeutics Europe (Bresso, Italy). Each remaining anthracenedione was synthesised as described [20] by Brad E. Sleebs and Keith G. Watson (Walter and Eliza Hall Institute of Medical Research, Melbourne, Australia). Calf thymus DNA was purchased from Worthington Biochemical Corporation (Lakewood, NJ). PhosphoDetect™ α-H2AX (pSer^{139}) rabbit antibody was purchased from Merck (Darmstadt, Germany). NuPAGE® 10% Bis-Tris gels and secondary Alexa Fluor® 488 goat α-rabbit antibody was obtained from Invitrogen (Carlsbad, CA). Rabbit α-Chk1 (pSer^{345}), rabbit α-Chk2 (pThr^{68}) and secondary goat α-rabbit HRP-linked antibody were obtained from Cell Signalling Technology (Beverly, MA). Protease inhibitor cocktail, PhosSTOP Phosphatase inhibitor cocktail and Lumi-Light Western Blotting substrate were from Roche (Mannheim, Germany). A Bio-Rad DC™ protein assay kit was purchased from Bio-Rad (Hercules, CA) and Immobilon transfer membrane was from Millipore (Billerica, MA). Human TOP2α was purchased from USB Corp. (Cleveland, Ohio) and its substrate kinetoplast DNA was from TopoGEN (Port Orange, FL). The remaining chemicals and reagents were of analytical grade. Distilled water passed through a four stage Milli-Q purification system was used to prepare all solutions.

2.2. Drugs

All anthracenedione stock solutions (stored at −20 °C) were prepared by dissolving each in Milli-Q water to an approximate concentration of 2 mM. Precise concentrations of each drug were determined spectrophotometrically using ε = 19,200 M^{-1} cm^{-1} at 608 nm and ε = 16,500 M^{-1} cm^{-1} at 641 nm for 5,8-dihydroxy-anthracenediones and 2-aza-anthracenediones, respectively. UCN-01 (1 mM) was prepared in DMSO and stored at −20 °C. Suramin and N-acetyl-L-cysteine were freshly dissolved in Milli-Q water on the day of each experiment.

2.3. Competitive ethidium displacement assay

A competitive ethidium displacement assay was performed as described previously [29]. In brief, serial aliquots of drug solution were added to a fluorimeter cell containing 1.30 μM ethidium bromide and 1.87 μM_{bp} calf thymus DNA in 1× TE (pH 8.0) and the fluorescence of the ethidium reporter monitored throughout. Fluorescence was measured using excitation and emission wavelengths of 530 and 605 nm, respectively, on a Perkin-Elmer LS50B fluorimeter at ambient temperature. The titration continued until the fluorescence was at least 50% of the original control value. The drug concentration that generated a 50% decrease in fluorescence (C_{50} value) was subsequently used to calculate an apparent binding constant (K_{app}) as detailed by Jenkins [29].

2.4. In vitro *kinetoplast DNA decatenation assay*

The *in vitro* kinetoplast DNA decatenation assay was performed essentially as described by Haldane and Sullivan [30]. Briefly, each reaction typically comprised human topoisomerase IIα (3 U), catenated kinetoplast DNA (325 ng) and various concentrations of each anthracenedione in reaction buffer (10 mM Tris–HCl pH 7.9, 50 mM NaCl, 50 mM KCl, 5 mM $MgCl_2$, 0.1 mM EDTA, 2.5% glycerol, 1 mM ATP, 0.015 mg/mL BSA). Reactions were incubated at 37 °C for 30 min, terminated with stopping solution (2% SDS, 0.05% bromophenol blue, 50% glycerol) and the DNA samples subsequently resolved through a 1% agarose gel (containing 0.5 μg/mL ethidium bromide) by electrophoresis. DNA samples were visualised and photographed under UV illumination.

2.5. Flow cytometry for cellular drug uptake

Following drug treatment, cells were harvested and analysed immediately using a FACSCanto II flow cytometer (BD Biosciences, San Jose, CA) incorporating a red laser line (633 nm) which was used for sample excitation. Drug-induced cellular fluorescence was collected using a 660/20 BP filter. Fifty thousand events were collected per sample and gated using forward- versus side-scatter to eliminate debris and cell doublets. The median fluorescence intensity of each sample population was calculated using FCS Express (De Novo Software, Los Angeles, CA) and was used as a measure of cellular drug uptake.

2.6. Analysis of apoptosis and cell cycle distribution by flow cytometry

Drug-treated cells were harvested, fixed with 70% ethanol and stored at −20 °C until required. Following fixation, cells were subjected to a PBS wash and then resuspended in a DNA staining solution comprising 2.5 μg/mL propidium iodide and 50 μg/mL RNase A in PBS. Samples were incubated at 37 °C for 30 min away from light and then analysed on a FACSCanto II flow cytometer. A blue 488 nm laser line was employed for propidium excitation and red fluorescence was measured using a 670 LP filter. Samples (10,000 events were collected per sample) were gated to exclude cell doublets and higher aggregates by applying a red fluorescence intensity-area versus -width dot plot.

2.7. Alkaline comet assay

The alkaline comet assay was performed as described by Swift et al. [31]. Briefly, drug-treated cells were harvested, mixed with molten low gelling temperature agarose (Type VII) and subsequently spread and allowed to set on a glass slide pre-coated with agarose. Gel-embedded cells were lysed in ice-cold lysis buffer [100 mM EDTA, 2.5 M NaCl, 10 mM Tris–HCl (pH 10.5), 1% Triton X-100] for 1 h and then subjected to 4× 15 min washes with ice-cold Milli-Q water. Samples were then submerged in chilled alkali electrophoresis buffer (1 mM EDTA, 300 mM NaOH) for 1 h and then subjected to electrophoresis (30 V) for 30 min at 4 °C. Neutralisation buffer [500 mM Tris–HCl (pH 7.5)] was subsequently added and then washed away with 2× 10 min PBS (pH 7.4) washes. Samples were subsequently stained twice with 2.5 μg/mL propidium iodide for 5 min each, rinsed with Milli-Q water and visualised using epi-fluorescence microscopy. The olive tail moment (OTM; [31]) of 50 individual cells was scored using Komet software (Kinetic Imaging, Nottingham, UK) to yield the average OTM for each sample.

2.8. Immunocytochemical detection of γH2AX by flow cytometry

The detection of γH2AX was based on the method described by MacPhail et al. [32]. Following detachment, drug-treated cells were fixed with 70% ethanol and stored at −20 °C for at least 12 h. On the day of analysis, cells were washed with cold TBS (pH 7.4) and then permeabilised with 1× TFX (TBS, 4% foetal calf serum, 0.1–0.25% Triton X-100) for 10 min on ice. Cells were subsequently incubated and mixed (200 rpm) with α-H2AX (pSer^{139}) rabbit antibody (1:500–1:800 in 1× TFX) for 2 h at room temperature. Following the removal of primary antibody using two washes with 1× TFX, samples were exposed to a secondary Alexa Fluor 488 goat anti-rabbit antibody (1:200 in 1× TFX) while shaking at room temperature (200 rpm) for 1 h away from light. Unbound secondary antibody was removed with a final 1× TFX wash and

the samples stained with 5 μg/mL propidium iodide in 1× TFX. Samples were analysed on a FACSCanto II flow cytometer incorporating a blue laser line (488 nm) which was used for sample excitation. Green and red fluorescence was collected using the 530/30 BP and 670 LP filters, respectively. Ten thousand events were collected per sample and gated using forward- versus side-scatter to eliminate debris and cell doublets.

2.9. Immunocytochemical detection of γH2AX by confocal microscopy

Samples were prepared for confocal microscopy as for flow cytometry, with some modifications. Following the removal of unbound secondary antibody with two independent washes in 1× TFX (propidium iodide staining was omitted), samples were deposited on poly-L-lysine coated coverslips and allowed to attach. Each sample was mounted and sealed in preparation for microscopy using an inverted Leica TCS-SP2 confocal system equipped with a 63× oil immersion objective and a 488 nm argon laser line for sample excitation. Fluorescence was detected from 500 to 580 nm. Confocal images were collected using Leica SP2 imaging software and subsequently processed using NIH ImageJ version 1.43u software (http://rsb.info.nih.gov/ij).

2.10. Western blot analysis

Following detachment, drug-treated cells were washed once with ice-cold 1 mM PMSF in PBS (pH 7.4) and then resuspended in a lysis solution comprising 50 mM Tris–HCl (pH 7.5), 150 mM NaCl, 1% nonidet P-40, 1× protease inhibitor and phosphatase inhibitor cocktail, 10 μg/mL aprotinin and 1 mM PMSF and then incubated on ice for 30 min. The total protein content from each cell lysate was quantitated using a Bio-Rad DC protein assay kit according to the manufacturer's protocol. Protein samples (40 μg) were subjected to Western blot analysis as detailed previously [33] with the following modifications. Membranes were initially exposed to either 1:500 α-Chk1 (pSer^{345}), 1:1000 α-Chk2 (pThr^{68}) or 1:2000 α-actin primary antibodies followed by exposure to 1:1000 secondary HRP-conjugated antibody for 2 h at room temperature.

2.11. Morphological analysis of mitotic catastrophe

Following drug treatment, both adherent and floating cells were harvested and then fixed in 4% paraformaldehyde in PBS for 20 min at ambient temperature. Samples were subsequently washed once with PBS, deposited on a glass slide pre-coated with poly-L-lysine and allowed to adhere for 30 min. Glass slides were washed twice with PBS and the cells gently lysed by adding 0.1% Triton X-100 in PBS for 5 min at room temperature. Cell nuclei were stained with 1 μg/mL Hoechst 33258 for 30 min. Following the removal of free stain with a final round of three PBS washes, samples were sealed and analysed using an Olympus 1X81 epi-fluorescence microscope. Cells harbouring multiple nuclei (≥3) were scored as multinucleated, a morphological hallmark of mitotic catastrophe [28]. A minimum of 200 cells was scored per sample.

2.12. Cell culture

The breast adenocarcinoma cell line MDA-MB-231 and PC-3 prostate cancer cells were obtained from Peter MacCallum Cancer Centre, Melbourne, Australia. Human promyelocytic leukaemia HL-60 cells and the mitoxantrone-resistant variant line HL-60/MX2 were purchased from the American Type Culture Collection (Rockville, MD). A2780 ovarian carcinoma cells were acquired from Dr Rosanna Supino (Istituto Nazionale Tumori, Milan, Italy). All cells were maintained at sub-confluent levels in RPMI 1640 media (Invitrogen, Carlsbad, CA) supplemented with 10% foetal calf serum (Trace Scientific, Melbourne, Australia) at 37 °C in a humidified 5% CO_2 atmosphere. MDA-MB-231 cells (2×10^5 per well) were typically seeded and allowed to attach overnight before drug treatment the following day whereas HL-60 cells were routinely treated on the day of seeding ($1.5–2 \times 10^5$ cells per well). The details of each drug treatment are specified in each figure legend.

2.13. Growth inhibition assay and evaluation of drug synergy

Cellular growth inhibition was evaluated using an MTT assay, a colourimetric-based assay whereby metabolically active, viable cells reduce the MTT tetrazolium salt to an intensely coloured formazan product that can be measured spectrophotometrically [34]. The assay was performed as described previously [35] with modifications. MDA-MB-231 cells were originally seeded into 96-well plates at a density of 3000 cells per well whereas both A2780 and PC-3 cells were seeded at 4000 cells per well. The details of each treatment are specified in each figure and table legend. The effect of combining various anthracenediones with UCN-01 on cellular growth inhibition was evaluated by calculating the combination index (CI) as described by Chou and Talalay [36].

3. Results

Mitoxantrone was originally developed with structural features that were anticipated to favour intercalative binding with DNA. Given the similar molecular structure shared by mitoxantrone and the 5,8-dihydroxy-anthracenediones, differing only in the length and composition of their side-chains, the DNA binding properties of the anthracenedione analogues were initially investigated.

3.1. DNA binding properties of the 5,8-dihydroxy-anthracenediones

The binding of 5,8-dihydroxy-anthracenedione analogues to calf thymus DNA *in vitro* was analysed by a competitive ethidium displacement assay. A C_{50} value, defined as the anthracenedione concentration that yielded a 50% decrease in the fluorescence of the initial ethidium–DNA complex, was determined for each compound and used to a generate a K_{app} (Table 1), an apparent equilibrium binding constant. The K_{app} values presented in Table 1 indicate that all 5,8-dihydroxy-anthracenediones demonstrated a remarkable affinity for calf thymus DNA comparable to mitoxantrone, generally considered a strong DNA-interactive agent [9]. Collectively, there was no considerable quantitative difference in K_{app} values amongst the 5,8-dihydroxy-anthracenedione group (ranging from 8.43 to 10.2×10^7 M^{-1}, Table 1), suggesting that the lengths of both side-chains has little influence on DNA binding at equilibrium *in vitro*.

3.2. Growth inhibition properties of the 5,8-dihydroxy-anthracenediones

Next, the growth inhibitory properties of the various anthracenediones were evaluated in A2780 ovarian and PC-3 prostate cancer cells by an MTT assay (as described in Section 2). Following the exposure of both cell lines to a range of anthracenedione concentrations continuously for 72 h, an IC_{50} was determined for each compound. Table 1 demonstrates that M2 was the most potent growth inhibitory compound in A2780 and PC-3 cell lines (36 and 280 nM, respectively), followed clearly by M3 (140 and 2800 nM) and then M4 (1600 and 4700 nM). M5 was the least effective at inducing growth inhibition in both A2780 and PC-3 cells (Table 1, 7600 and 11,000 nM, respectively). Thus, there was a very clear inverse relationship in growth inhibition by the newly

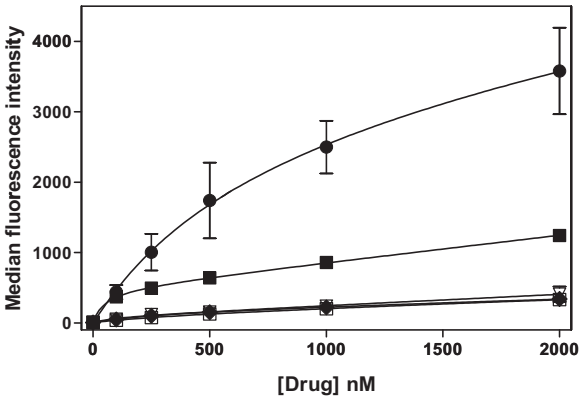

Fig. 1. The differential penetration of MDA-MB-231 cells by various anthracenediones. MDA-MB-231 cells were exposed to 0–2000 nM of either mitoxantrone (open squares), M2 (solid circles), M3 (solid squares), M4 (solid diamonds) or M5 (inverted open triangles) for 90 min. Cells were harvested and immediately analysed for drug uptake by flow cytometry as described in Section 2. The median drug-induced fluorescence intensity of each cellular population is expressed as a function of drug concentration. Error bars represent the SEM of at least three independent experiments.

prepared 5,8-dihydroxy-anthracenediones and their aliphatic side-chain lengths. Importantly, a similar inverse relationship was independently identified by Mansour et al. ([20] and Table 1) in HL-60 cells, indicating that the inverse relationship was not cell-type specific but a common trend amongst three different cell lines. Table 1 also highlights that M2-induced growth inhibition was at least equivalent to the clinically applied drug mitoxantrone (IC_{50} values ranging from 29 to 290 nM) and demonstrated significantly greater growth inhibition relative to pixantrone (IC_{50} 1800 nM) in PC-3 cells.

3.3. Anthracenediones differentially penetrate cultured cancer cells depending on their side-chain length

Although the assay cannot readily differentiate drug uptake from DNA intercalation, the drug-induced cellular fluorescence emitted by mitoxantrone and its analogues has successfully been employed in conjunction with flow cytometry to measure drug penetration and retention in whole cell populations [37]. Cellular fluorescence induced by all 5,8-dihydroxy-anthracenediones was readily detectable by flow cytometry throughout the concentrations that were analysed (0–2000 nM). Fig. 1 demonstrates that drug-associated fluorescence was highly sensitive to the chain length of each 5,8-dihydroxy-based compound. At a fixed median fluorescence intensity of 500 arbitrary units, M2 was the most readily detectable at 100 nM, closely followed by M3 at approximately 250 nM. M4, M5 and mitoxantrone each penetrated MDA-MB-231 cells relatively poorly with concentrations in excess of the maximum tested (2000 nM) required to achieve 500 arbitrary units (Fig. 1).

3.4. Drug side-chain length is a major determinant of anthracenedione-induced DNA damage

An alkaline comet assay was employed in a preliminary screen for anthracenedione-induced DNA damage. The comet assay provides a very sensitive qualitative and quantitative measurement of DNA damage in individual cells. Following an initial 2 h exposure to varying concentrations of each anthracenedione, the DNA integrity of individual MDA-MB-231 cells was visualised and quantitated using the comet assay. Mock-treated cells (Fig. 2A) were consistently represented by intensely staining, largely spherical nuclei, indicating that their nuclear DNA remained intact. The extent of visual damage in the comet tails of drug-exposed cells was highly drug-dependent and ranged from extensive (12.5 nM M2, Fig. 2B) to modest (12.5 nM mitoxantrone, Fig. 2C) to absent (1000 nM M5, Fig. 2D). Quantitation of the OTM of each comet demonstrated a striking association of drug-induced DNA damage with side-chain length. At a fixed OTM level of 5, M2 was the most potent inducer of DNA damage at approximately 10 nM (Fig. 2E). The parent compound mitoxantrone was next at about 50 nM, followed by M3 at 200 nM (Fig. 2E). Both M4 and M5 failed to induce a level of 5 OTM at any of the concentrations tested (>2000 nM, Fig. 2E), however M4 conspicuously induced greater damage than M5, which generated no detectable damage above background, even at the highest concentration (Fig. 2E). Thus, with the obvious exception of mitoxantrone, a clear inverse relationship existed between drug side-chain length and DNA damage induction.

The DNA damage induced by a 2-aza-anthracenedione (i.e. pixantrone) family of compounds generated a comparable trend, although not as prominent. Pixantrone, bearing the shortest pair of side-chains (Table 1), clearly induced the most DNA damage with about 1000 nM generating an OTM of 5 (Fig. 2F). P3, P4 and P5 (the 2-aza-anthracenedione equivalents of M3, M4 and M5, respectively) stimulated little or no detectable DNA damage at any of the concentrations tested (Fig. 2F). Notably, the anthracenediones belonging to the mitoxantrone family consistently induced greater DNA damage than the corresponding 2-aza-analogue bearing the same side-chain length (Fig. 2E and F), indicating that the chromophore configuration is also critical in DNA damage induction.

3.5. Anthracenedione-induced γH2AX is also dependent on compound side-chain composition

The immunocytochemical detection of γH2AX provided an ideal opportunity to independently confirm the pattern in anthracenedione-induced DNA damage identified by the alkaline comet assay. MDA-MB-231 cells were exposed for 2 h to either mitoxantrone, M2 or M5 and then assayed for γH2AX formation. Both M2 and mitoxantrone readily induced γH2AX in MDA-MB-231 cells, with very low drug concentrations (approximately 10 and 70 nM, respectively) sufficient to induce a 50% level of γH2AX induction (Fig. 3A). In contrast, M5 failed to induce any detectable γH2AX above background throughout the entire concentration range (0–2000 nM, Fig. 3A). Again, anthracenedione side-chain composition and length was a major determinant in the induction of γH2AX, a notion consistent with the trend in DNA damage detected by the comet assay (Fig. 2).

3.6. Cultured cancer cells in G1 and S phase are most susceptible to anthracenedione-induced γH2AX

The analysis of anthracenedione-induced γH2AX expression by flow cytometry was further scrutinised in the context of cell cycle position. Based on DNA content, the total cell population of each sample in Fig. 3A was divided into either G1, S or G2/M subpopulations and the percentage of γH2AX-positive cells in each phase presented as a function of M2 (Fig. 3B) or mitoxantrone (Fig. 3C) concentration. MDA-MB-231 cells positioned in S phase, followed by cells in G1 phase, were clearly the most susceptible to M2-induced γH2AX expression at low concentrations (0–25 nM, Fig. 3B). Cells positioned in G2/M were the least sensitive to γH2AX induction at these low concentrations (0–25 nM, Fig. 3B), however the phase specificity was lost at higher M2 concentrations (50–100 nM, Fig. 3B), where H2AX phosphorylation levels were equally saturated in all phases. Cells exposed to mitoxantrone displayed a comparable cell cycle specificity in γH2AX induction. Again, both S

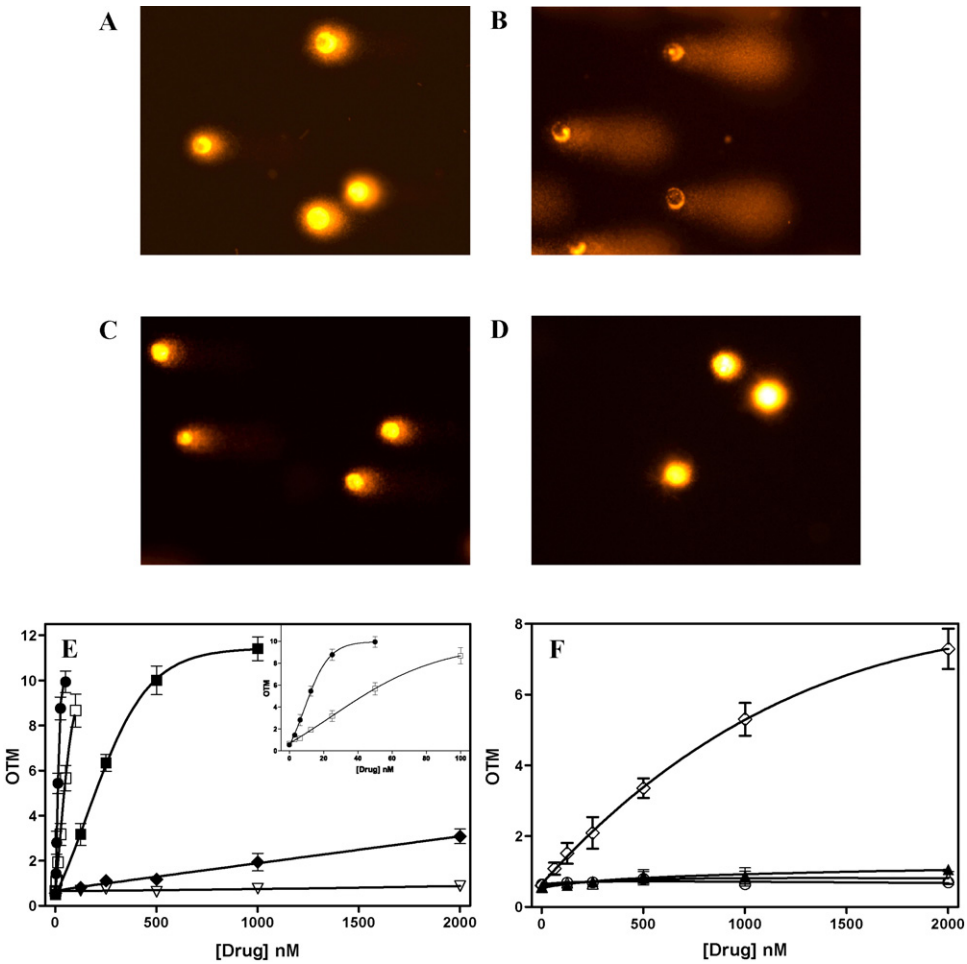

Fig. 2. Anthracenediones differentially induce DNA damage depending on their side-chain length. MDA-MB-231 cells were exposed to various anthracenediones at a range of concentrations (0–2000 nM as indicated) for 2 h, harvested and then subjected to an alkaline comet assay as described in Section 2. Cells that were either (A) mock-treated or exposed to (B) 12.5 nM M2, (C) 12.5 nM mitoxantrone or (D) 1000 nM M5 were subsequently stained with propidium iodide and visualised using epi-fluorescence microscopy. Original magnification 200×. The average OTM ± SEM ($n \geq 2$ independent experiments) was quantitated and is expressed as a function of drug concentration in (E) for M2 (solid circles), mitoxantrone (open squares), M3 (solid squares), M4 (solid diamonds), M5 (inverted open triangles) and in (F) for pixantrone (open diamonds), P3 (solid triangles), P4 (open hexagons) and P5 (open triangles). The inset of (E) shows an expansion of the concentration range from 0 to 100 nM for M2 and mitoxantrone.

and G1 phase cells were the most sensitive to mitoxantrone-induced γH2AX, however, there was very little difference in γH2AX levels between the two phases at all concentrations (0–100 nM, Fig. 3C). Cells positioned in G2/M phase were poorly predisposed to H2AX phosphorylation stimulated by mitoxantrone, with these cells displaying a very modest response at all concentrations (0–100 nM, Fig. 3C).

3.7. Anthracenedione-induced DNA damage is most likely not mediated by reactive oxygen species (ROS)

Next, it was necessary to determine the mechanism of anthracenedione-induced DNA damage. Although it is a poor substrate for the pathway, mitoxantrone can undergo redox cycling and generate ROS [38], a species reportedly responsible, at

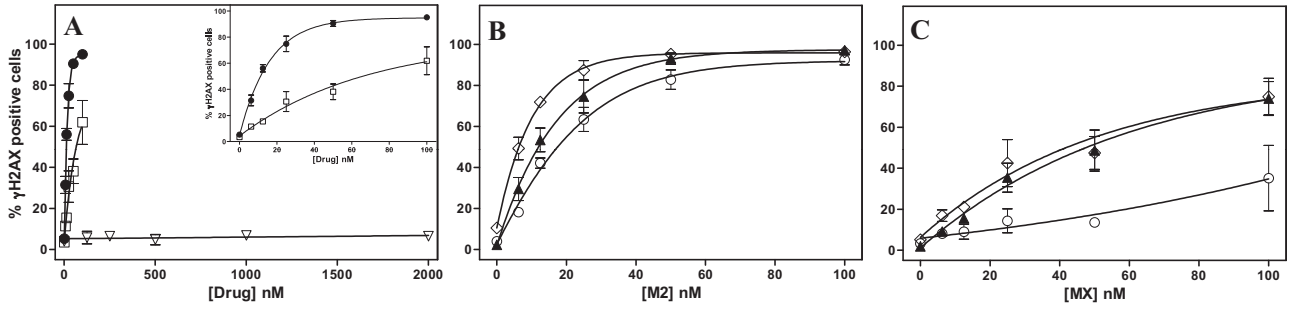

Fig. 3. The induction of γH2AX by various anthracenediones. (A) MDA-MB-231 cells were treated with 0–2000 nM of either mitoxantrone (open squares), M2 (solid circles) or M5 (inverted open triangles) for 2 h, harvested, fixed and processed for the immunocytochemical detection of γH2AX by flow cytometry. The fraction of γH2AX-positive cells in the whole cell population is presented as a function of anthracenedione concentration. The total cell population of each sample in (A) was divided into either G1 (solid triangles), S (open diamonds) or G2/M (open circles) subpopulations and the percentage of γH2AX-positive cells in each phase is presented as a function of (B) M2 or (C) mitoxantrone concentration. Error bars represent the SEM of a minimum of two independent experiments.

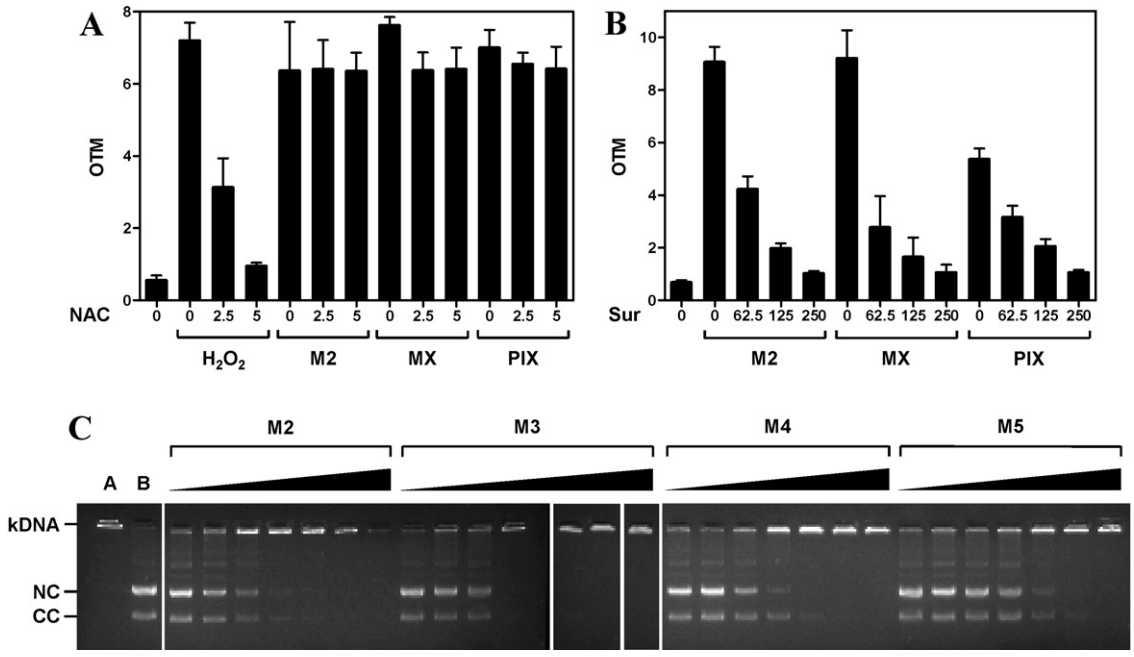

Fig. 4. DNA damage induction by anthracenediones is not mediated via the generation of ROS, yet anthracenediones can impair the function of TOP2. Human breast cancer MDA-MB-231 cells were pre-exposed to either (A) 0–5 mM N-acetyl-cysteine (NAC) or (B) 0–250 μM suramin (Sur) as indicated for 30 min and then 50 μM H_2O_2, 25 nM M2, 100 nM mitoxantrone (MX) or 1000 nM pixantrone (PIX) for 2 h. Cells were subsequently harvested and processed using the alkaline comet assay as described in Section 2. Each column represents the average OTM ± SEM of at least two independent experiments. (C) Catenated kDNA (325 ng) was incubated with 0.25, 0.5, 1, 2.5, 5, 10 or 20 μM (denoted by a solid triangle) of each anthracenedione and human TOP2α (3 U) for 30 min at 37 °C. Reactions were terminated and then subjected to agarose electrophoresis as described in Section 2. Lane A is a control that represents catenated kDNA not exposed to TOP2α. Lane B indicates the fully decatenated nicked (NC) and closed (CC) DNA mini-circles released by TOP2 in the absence of anthracenediones. The concentration of each anthracenedione required for 50% inhibition of TOP2 decatenation activity is represented in Table 1.

least in part, for mitoxantrone-mediated DNA damage [39]. MDA-MB-231 cells were initially treated (0, 2.5 or 5 mM) with the ROS scavenger N-acetyl-L-cysteine (NAC) for 30 min, exposed to a variety of DNA damaging agents including hydrogen peroxide (H_2O_2), M2, mitoxantrone or pixantrone for 2 h and then analysed for DNA damage using the alkaline comet assay. Cells pre-exposed with rising NAC concentrations (2.5 and 5 mM, Fig. 4A) were increasingly resistant to H_2O_2-induced DNA, damage suggesting that NAC provided a protective effect against the ROS generated by H_2O_2. In contrast, M2, mitoxantrone and pixantrone-induced levels of DNA damage remained completely unaffected by pre-exposure to 2.5 or 5 mM NAC (Fig. 4A), indicating that anthracenedione-mediated DNA damage is independent of ROS in MDA-MB-231 cells.

In a parallel series of experiments, NAC was substituted for pre-exposure for 30 min with 0–250 μM suramin, a TOP2 inhibitor [40]. Importantly, incubation of MDA-MB-231 cells with suramin (up to 250 μM) alone failed to induce any detectable DNA damage above background by the comet assay (data not shown). Suramin was particularly effective in shielding against DNA damage induced by M2, mitoxantrone and pixantrone throughout the entire concentration range (62.5, 125 and 250 μM, Fig. 4B). Collectively, the results indicate that TOP2 may be involved in the generation of anthracenedione-induced DNA damage.

3.8. The 5,8-dihydroxy-anthracenediones can function as TOP2α catalytic inhibitors in vitro

Despite extensive efforts to detect TOP2-mediated DNA scission by anthracenediones, only very weak cleavage activity by mitoxantrone, and none by M5, was achieved using an *in vitro* cleavage assay (data not shown). Accordingly, an *in vitro* kinetoplast DNA decatenation assay was subsequently utilised to examine the TOP2α inhibition profile of the 5,8-dihydroxy-anthracenediones. kDNA is typically catenated in large networks and can be decatenated into DNA mini-circles (represented as NC and CC in lane B, Fig. 4C) through the catalytic activity of TOP2α. The inhibition of TOP2α catalytic activity can be reflected by the absence of DNA mini-circles and a concomitant retention of the large kDNA network within the agarose gel well (lane A, Fig. 4C). Fig. 4C shows that all 5,8-dihydroxy-anthracenediones inhibited TOP2α catalytic activity at some level, however there was a clear difference in their potencies. The anthracenedione concentration required for 50% inhibition of TOP2 decatenation activity (TOP2 IC_{50}) was quantitated and the data are presented in Table 1. M2 and M3 were the most potent inhibitors of TOP2 decatenation activity with TOP2 IC_{50} values of 1.3 and 1.4 μM, respectively (Table 1 and Fig. 4C). At a TOP2 IC_{50} concentration of 3.2 μM, M4 was the next most potent compound (Table 1 and Fig. 4C), while the poorest inhibitor was M5, displaying a TOP2 IC_{50} value of 5.6 μM (Table 1 and Fig. 4C).

3.9. TOP2 is a likely requirement for anthracenedione-induced cellular DNA damage and subsequent apoptosis

Despite its activity as a TOP2 catalytic inhibitor, suramin has demonstrated several other cellular effects including the impairment of various kinases and growth factor–receptor interactions [40], factors that may have influenced its attenuation of anthracenedione-induced DNA damage (Fig. 4B). The involvement of TOP2 in anthracenedione-induced cellular DNA damage was confirmed by utilising the parental HL-60 cell line and its mitoxantrone-resistant variant HL-60/MX2. The HL-60/MX2 line, originally generated by continuous exposure of HL-60 cells to mitoxantrone, has no detectable TOP2β and a truncated form of the α isozyme distributed in the cytoplasm [41]. Both cell lines were exposed to various 5,8-dihydroxy-anthracenediones (0–4000 nM) for 2 h, harvested and then analysed for DNA damage using the alkaline comet and γH2AX assays or apoptosis. Relative to the anthracenedione-induced pattern in DNA damage in MDA-MB-231 cells (Fig. 2E), Fig. 5A shows that the striking pattern

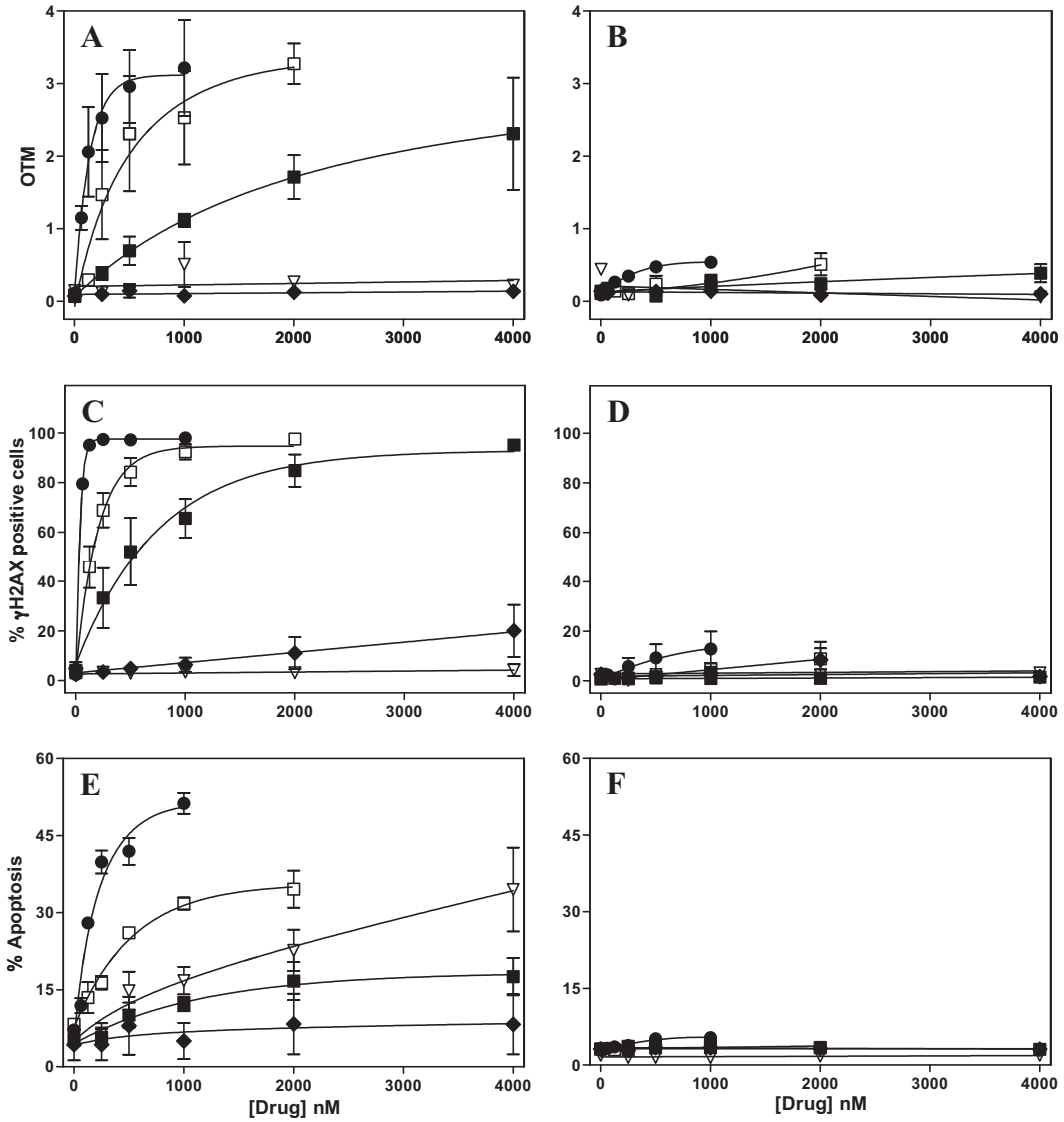

Fig. 5. TOP2-compromised HL-60/MX2 cells are resistant to anthracenedione-induced DNA damage and apoptosis. Both HL-60 (A and C) and HL-60/MX2 (B and D) cells were treated with various anthracenediones (0–4000 nM) for 2 h, harvested and then processed using alkaline comet (A and B) and γH2AX (C and D) assays as described in Section 2. In a separate set of experiments, HL-60 (E) and HL-60/MX2 (F) cells were exposed to drug as described above, however the treatment time was extended to 6 h. Symbols representing various anthracenediones are the same as described in Fig. 1. Cells were harvested, fixed and analysed for apoptosis-associated DNA fragmentation by flow cytometry as described in Section 2. Error bars represent the SEM of at least two independent experiments for all assays.

identified by the comet assay is maintained in parental HL-60 cells. In complete contrast, OTM levels in drug-treated HL-60/MX2 cells were essentially undetectable throughout the entire concentration range of all anthracenediones (Fig. 5B), suggesting that DNA damage by the anthracenediones is mediated via TOP2.

In an effort to independently substantiate the contrasting DNA damage responses in parental and variant lines, drug-treated cells were processed for γH2AX expression. Again, the familiar pattern in anthracenedione-induced DNA damage was evident in parental HL-60 cells (Fig. 5C), with M2 inducing γH2AX most prominently, followed by mitoxantrone, M3, M4 and finally M5 (Fig. 5C). TOP2-compromised HL-60/MX2 cells were clearly less susceptible to γH2AX induction by all anthracenediones (Fig. 5D), a result that corresponds well with the virtual absence of DNA damage in these same cells revealed by the comet assay (Fig. 5B). Collectively, these results implicate TOP2 as a key mediator of DNA damage induced by the anthracenediones.

Apoptosis-associated DNA fragmentation, detected by propidium iodide staining for sub-G1 DNA content, was next investigated as a potential secondary consequence of anthracenedione-induced DNA damage. Both parental and variant cell lines were incubated with various anthracenediones (0–4000 nM) for 6 h, harvested and then analysed for sub-G1 DNA content by flow cytometry. Fig. 5E shows that the DNA fragmentation pattern induced by the various anthracenediones in HL-60 cells was highly similar to the pattern detected by both comet (Fig. 5A) and γH2AX (Fig. 5C) assays, suggesting a tight association between DNA damage induction and apoptosis. Significantly, apoptosis-associated DNA fragmentation by all anthracenediones was essentially absent in the variant HL-60/MX2 line (Fig. 5F), demonstrating a TOP2-dependent mechanism for anthracenedione-induced apoptosis.

3.10. Anthracenediones differentially induce γH2AX foci in wild-type HL-60 cells, but not in the variant HL-60/MX2 line

A variety of γH2AX immunofluorescence staining patterns have been identified and described including focus formation, pan-nuclear staining and apoptosis-associated "ring" structures that form a boundary along the nuclear periphery [42]. The pattern of

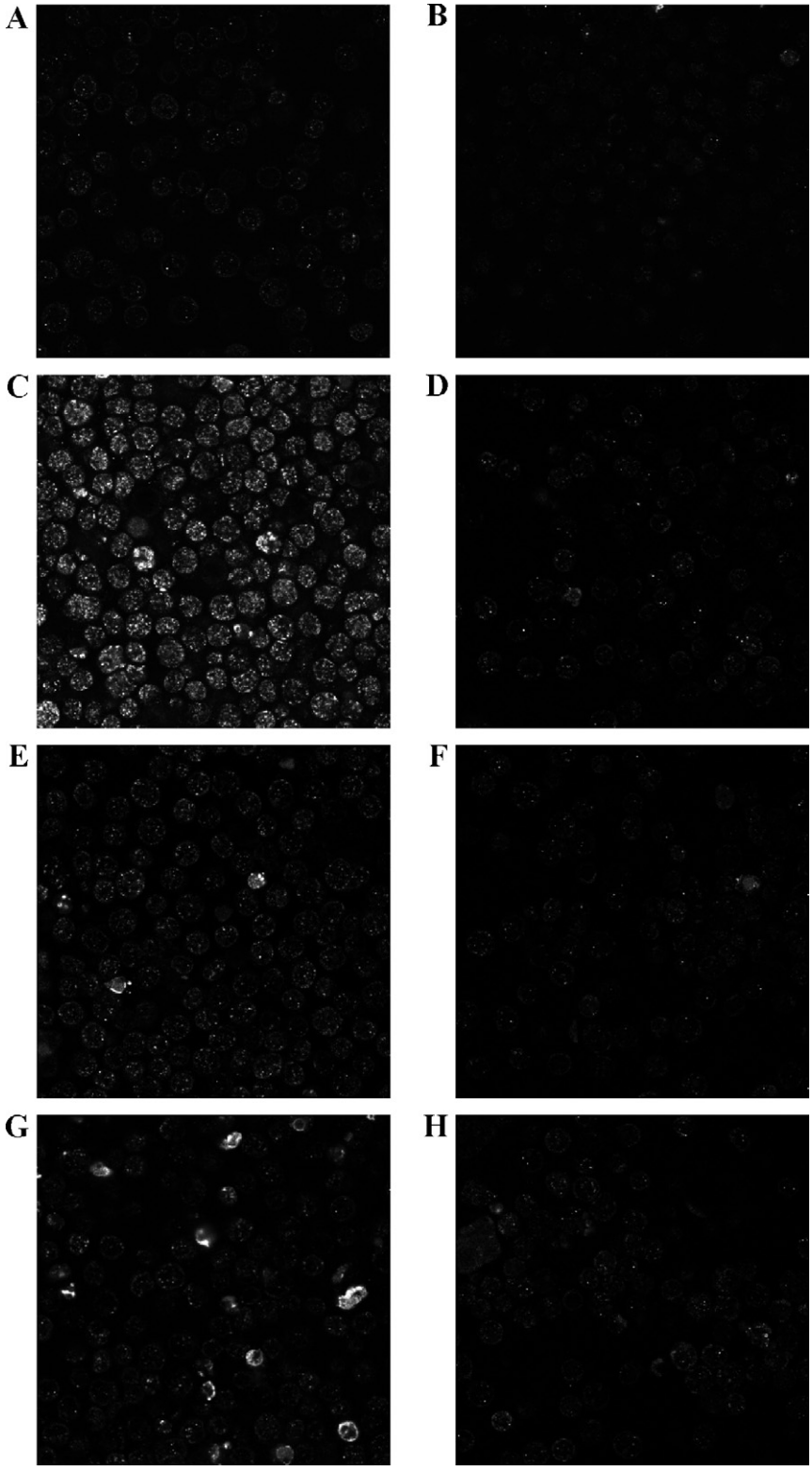

Fig. 6. Anthracenediones differentially induce γH2AX foci in wild-type HL-60 cells, but not in the variant HL-60/MX2 line. Parental HL-60 (A, C, E and G) and TOP2 defective HL-60/MX2 (B, D, F and H) cells were either mock-treated (A and B) or exposed to 25 nM M2 (C and D), 25 nM mitoxantrone (E and F) or 2000 nM M5 (G and H) for 2 h and then processed for γH2AX using immunofluorescence as described in Section 2. Confocal microscopy was used to capture the pattern of γH2AX immunofluorescent staining at 630× magnification for each image (A–H).

γH2AX induction by the various anthracenediones was subsequently explored by confocal microscopy. Both HL-60 and HL-60/MX2 cells were treated with various anthracenediones for 2 h, processed for γH2AX and then visualised by confocal microscopy. Fig. 6 demonstrates that mock-treated HL-60 and HL-60/MX2 cells (Figs. 6A and 7B) both harbour low background numbers of γH2AX foci. In contrast, parental HL-60 cells exposed to 25 nM M2 typically displayed distinct foci that were prominent and widespread throughout (Fig. 6C). Mitoxantrone-treated HL-60 cells (25 nM, Fig. 6E) exhibited similar focal structures, yet their

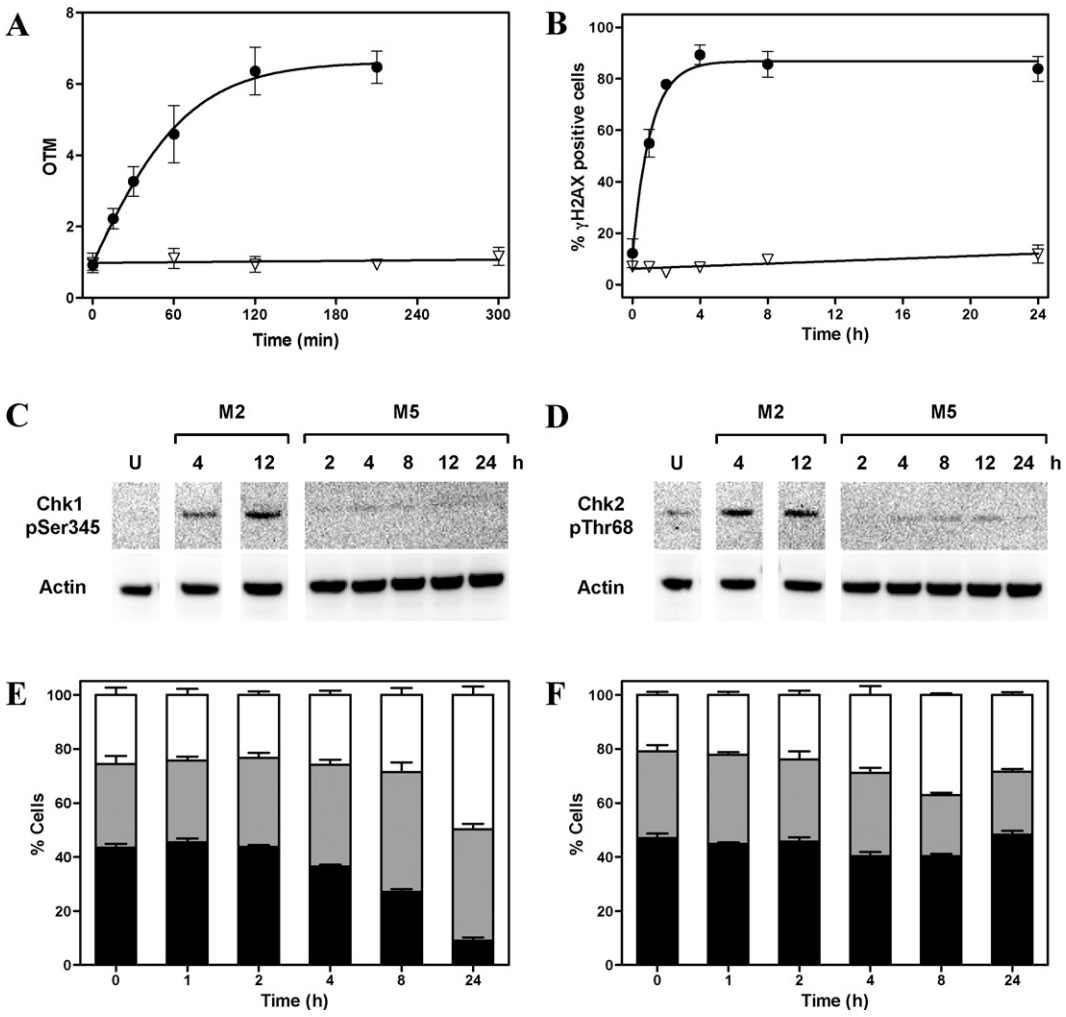

Fig. 7. M2, but not M5, efficiently activates the DNA damage response. (A–F) MDA-MB-231 cells were exposed to either 12.5 nM M2 (solid circles, A and B) or 2000 nM M5 (inverted open triangles, A and B) for increasing time periods and then subjected to analysis by (A) alkaline comet, (B) flow cytometry for γH2AX induction and Western blotting for (C) Chk1 ($pSer^{345}$), (D) Chk2 ($pThr^{68}$) and actin (C and D) as detailed in Section 2. U represents untreated control samples. All M2- and M5-treated samples in (B) were concurrently analysed by flow cytometry for cell cycle distribution (E and F, respectively) and divided into either G1 (solid black bars), S (grey bars) or G2/M (open bars) subpopulations. Error bars (A, B, E and F) represent the SEM of at least two independent experiments.

distribution throughout each cell was more limited relative to cells exposed to an equivalent M2 dose (Fig. 6C). M5 induced few γH2AX foci (2000 nM, Fig. 6G), however a select few cells exhibited intense γH2AX staining that may correspond with apoptosis-associated "ring" structures [42]. Most importantly, HL-60/MX2 cells exposed to either 25 nM M2, 25 nM mitoxantrone or 2000 nM M5 (Fig. 6D, F and H, respectively) all displayed few foci, indicating a role for TOP2 in the generation of drug-induced γH2AX foci.

3.11. M2, but not M5, efficiently induces DNA damage, subsequent G2/M arrest and activates cell cycle checkpoints

Given the clear disparity in M2- and M5-induced DNA damage, both were selected for further characterisation at a molecular level. MDA-MB-231 cells were exposed to either 12.5 nM M2 or 2000 nM M5 for increasing time periods and the level of cellular DNA damage was evaluated using the comet assay (Fig. 7A) and γH2AX induction (Fig. 7B). Fig. 7A reveals that 12.5 nM M2 induced DNA damage rapidly and in a time-dependent fashion where a maximal OTM was achieved within 2 h of M2 exposure. Conversely, 2000 nM M5 failed to induce detectable levels of DNA damage within 5 h (Fig. 7A). The pattern in γH2AX induction (Fig. 7B) was entirely consistent with these data (Fig. 7A). M2-induced γH2AX was both rapid and potent (Fig. 7B) reaching a steady maximal level of ~90% within 4 h, a level that was maintained over a 24 h period. In contrast, cells were essentially insensitive to M5-induced γH2AX (Fig. 7B) throughout the 24 h exposure. Although both comet and γH2AX assays were consistent in demonstrating a time-dependent trend for M2-induced DNA damage (Fig. 7A and B), there was a significant difference in the time required for the comet (2 h, Fig. 7A) and γH2AX (4 h, Fig. 7B) assays to achieve a steady-state level. The 2 h lag period may reflect processing of an initial lesion, presumably a concealed M2-induced TOP2 cleavage complex, detectable by the strong alkaline condition of the comet assay [43], to a secondary lesion in the form of a frank DSB coupled with γH2AX induction.

Next, the activation of two key cell cycle checkpoint kinases, Chk1 and Chk2, was evaluated by Western blot. Conspicuous levels of DNA damage induced by 12.5 nM M2 (Fig. 7A and B) were associated with an steady increase in the phosphorylation of Chk1 at serine 345 over 4 and 12 h of M2 exposure (Fig. 7C). Fig. 7D reveals that Chk2 was concomitantly phosphorylated at residue threonine 68, although maximal signal intensity was achieved within 4 h of M2 exposure, a level that remained over a 12 h period. At best, both Chk1 and Chk2 were very weakly phosphorylated at the corresponding residues in response to treatment with 2000 nM M5 throughout the 24 h exposure (Fig. 7C and D).

Activation through phosphorylation of Chk1 and Chk2 by M2 (Fig. 7C and D) indicated that the compound may induce subsequent G2/M arrest. Samples analysed for γH2AX induction presented in Fig. 7B were simultaneously monitored for DNA content by flow cytometry. Each M2- and M5-treated sample population in Fig. 7B was divided into either G1, S or G2/M phases based on DNA content and the phase distribution induced by 12.5 nM M2 and 2000 nM M5 is presented as a function of time in Fig. 7E and F, respectively. Treatment of MDA-MB-231 cells with 12.5 nM M2 continuously for 24 h initially manifested itself as an increase in the proportion of S phase cells by 4 h, a fraction that continued to increase thereafter (Fig. 7E). A small increase in the percentage of M2-treated cells in G2/M was initially detected at 8 h (∼25%) and continued to expand to ∼50% by 24 h (Fig. 7E). Collectively, the M2-induced changes in cell cycle distribution most likely reflect impaired S phase traverse and subsequent arrest in G2/M. A further notable feature of the M2-induced cell cycle distribution (Fig. 7E) was the absence of a G1 arrest throughout M2 exposure. Indeed, only a small fraction (∼10%) of M2-treated cells were positioned in G1 at 24 h M2 exposure (Fig. 7E), with the vast bulk (∼90%) either traversing S or arrested in G2/M (Fig. 7E).

Unlike M2, the cell cycle distribution of MDA-MB-231 cells incubated with 2000 nM M5 showed little distortion, relative to the 0 control time point, throughout 24 h of compound exposure (Fig. 7F). A mild increase in the fraction of G2/M cells (and a corresponding decrease in the percentage of S phase cells) was evident at 4 and 8 h of M5 exposure (Fig. 7F), yet even this small perturbation was largely absent at 24 h (Fig. 7F). The consistent absence of DNA damage (Fig. 7A and B), weak activation of Chk1 and Chk2 (Fig. 7C and D) and the very mild impairment of cell cycle distribution induced by M5 collectively suggests that M5 does not efficiently activate the DDR.

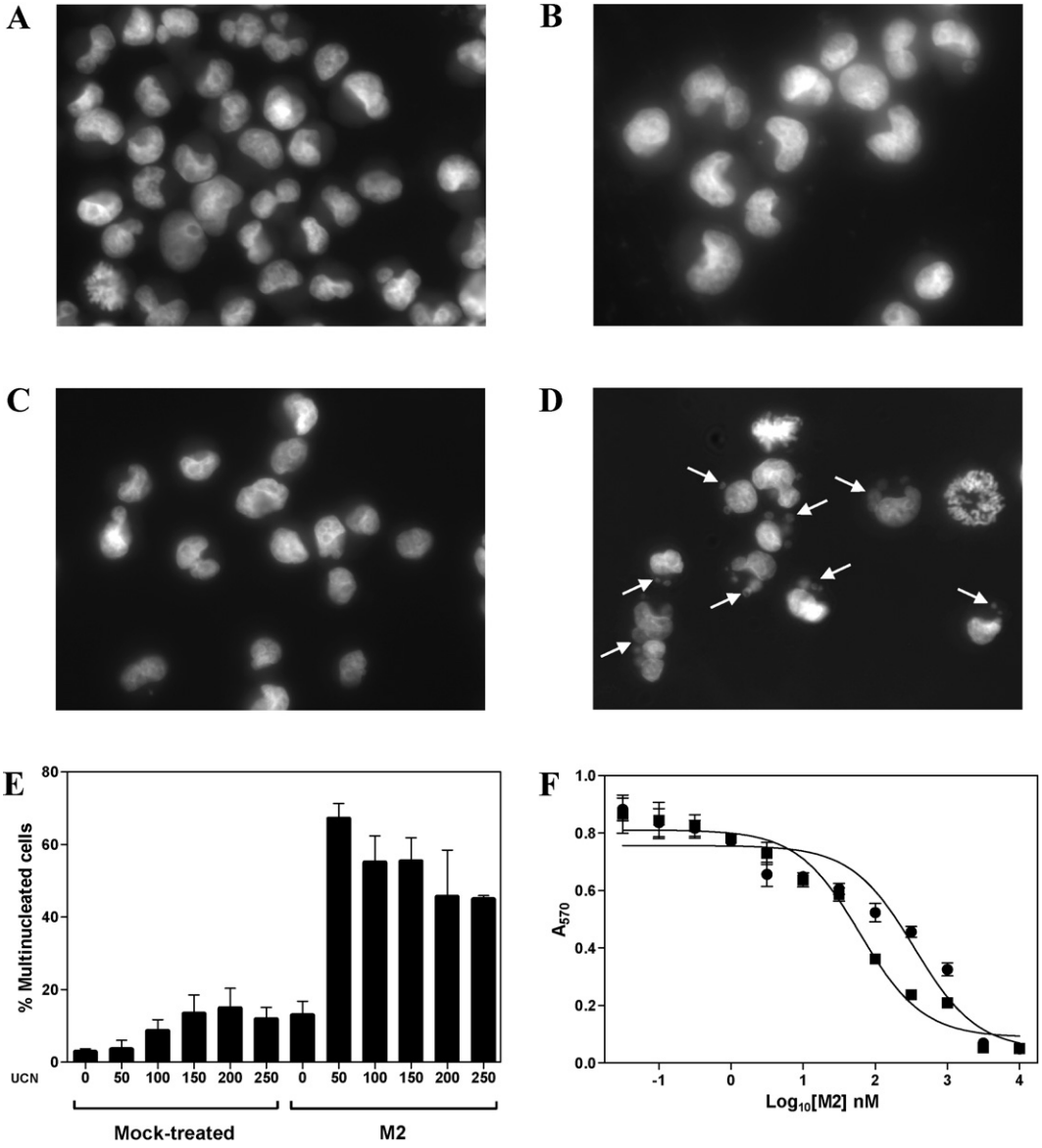

Fig. 8. Sequential treatment with M2 followed by UCN-01 induces cellular characteristics synonymous with mitotic catastrophe. (A–E) MDA-MB-231 cells were initially exposed to 12.5 nM M2 for 4 h, the compound removed and samples subsequently treated with UCN-01 (0–250 nM) for a further 20 h. The nuclear morphology of cells that were either (A) mock-treated or treated with (B) 12.5 nM M2, (C) 50 nM UCN-01 or (D) sequentially with 12.5 nM M2 followed by 50 nM UCN-01 was examined by epi-fluorescence microscopy. Arrows indicate cells harbouring multiple nuclei. Original magnification 640×. (E) The fraction of multinucleated cells in each sample was scored and is expressed as a function of UCN-01 concentration. Each column represents the average % of multinucleated cells ± SEM of three independent experiments. (F) A representative MTT growth inhibition curve of MDA-MB-231 cells initially treated with a range of M2 concentrations and subsequently mock-treated (solid circles) or exposed to UCN-01 (solid squares). Further treatment details are provided in the legend of Table 2. Error bars represent the standard deviation of four replicates of a single typical experiment.

3.12. Sequential treatment of MDA-MB-231 cells with M2 followed by UCN-01 induces widespread mitotic catastrophe and permits very strong synergism in growth inhibition

MDA-MB-231 cells were subjected to an initial pulse exposure of 12.5 nM M2 for 4 h, the compound removed and the cells incubated with UCN-01, a cell cycle checkpoint kinase inhibitor for a further 20 h. Examination of the nuclear morphology by microscopy revealed that the nuclei of mock-treated control cells (Fig. 8A) were mostly uniform with the chromatin distributed homogenously throughout, characteristics typical of normal cells. Exposure to 12.5 nM M2 alone (Fig. 8B) rendered the nuclei with a larger, more bloated morphology, yet the nuclei remained uniform and intact. Although the nuclei of cells treated with 50 nM UCN-01 alone (Fig. 8C) largely resembled mock-treated control cells (Fig. 8A), sequential treatment with M2 (12.5 nM) followed by UCN-01 (50 nM) generated cells containing multiple, multi-lobed and abnormally shaped nuclei (Fig. 8D), morphological characteristics synonymous with mitotic catastrophe [28].

Cells harbouring multiple nuclei (≥3) were scored as multinucleated and the fraction of multinucleated cells in each sample is presented in Fig. 8E. Populations of untreated cells typically presented with very low levels of multinucleated cells (~3%, Fig. 8E). Exposure of cells to UCN-01 alone (0–250 nM) yielded a small, but dose-dependent increase in cellular multinucleation (Fig. 8E). Treatment with 12.5 nM M2 alone also yielded a comparable increase in the percentage of multinucleated cells (~13%, Fig. 8E), however the introduction of 50 nM UCN-01 generated a very large enhancement in multinucleation (~67%, Fig. 8E). Interestingly, the introduction of increasing concentrations of UCN-01 (100–250 nM) essentially diminished the population of cells with multiple nuclei from ~67% to 45% (Fig. 8E), levels nonetheless well beyond those yielded by the corresponding single agent-treated controls.

Given the large enhancement in multinucleation mediated by sequential treatment with M2 and UCN-01, an MTT assay was utilised to evaluate the growth inhibition of MDA-MB-231 cells exposed to combination treatments. MDA-MB-231 cells were initially exposed to a variety of M2 concentrations for 4 h and then treated with UCN-01 for a further 20 h. Following drug treatment, the cells were re-incubated in drug-free medium for a further 48 h, and the viable cell fraction determined by an MTT assay. A representative growth inhibition curve, presented in Fig. 8F, indicates that M2 alone induced a level of 50% growth inhibition at ~500 nM, yet sequential treatment with UCN-01 yielded a 6–7-fold decrease in M2 IC_{50} to ~75 nM. A more thorough analysis of the interaction shared by M2 and UCN-01 in inducing growth inhibition was performed by calculating a combination index (CI, Table 2). M2 displayed strong synergy in MDA-MB-231 cells in combination with UCN-01 (CI = 0.30, Table 2), whereas the interaction of pixantrone, a 2-aza chemotype of M2, with UCN-01 was only slightly synergistic (CI = 0.86, Table 2). Mitoxantrone in particular exhibited the most intense interaction with UCN-01, yielding a CI of 0.26 in MDA-MB-231 cells (Table 2).

Table 2
Anthracenediones, particularly M2 and mitoxantrone, synergise strongly with the staurosporine analogue UCN-01 to inhibit the growth of MDA-MB-231 cells. MDA-MB-231 cells were initially subjected to a pulse exposure of either M2, mitoxantrone or pixantrone for 4 h at a variety of concentrations. Following the removal of anthracenedione, cells were incubated with UCN-01 at a fixed ratio of 4:1 (anthracenedione: UCN-01) for a further 20 h. UCN-01 was removed and the cells incubated in compound-free media for 48 h. The fraction of compound-induced growth inhibition in each sample was evaluated by an MTT assay as described in Section 2. The values represent the IC_{50} mean ± SEM of *n* independent experiments, where *n* is indicated in parentheses alongside. The data was subjected to isobologram analysis to determine the combination index.

Compound	Growth inhibition (IC_{50}) nM		Combination index
	Single agent[a]	Combination	
M2	480 ± 50 (3)	77 ± 11 (3)	0.30
Mitoxantrone	460 ± 70 (4)	66 ± 12 (4)	0.26
Pixantrone	14,000 ± 1200 (4)	470 ± 45 (4)	0.86

[a] Indicates that the IC_{50} of UCN-01 alone was 140 ± 20 nM.

4. Discussion

A good basis for the therapeutic development of the anthracenedione family of compounds is an initial characterisation of the mechanism that underpins the variation in their activity (Table 1). Two factors clearly emerged as likely determinants of their variation in biological activity. First, a modest inverse relationship was established between growth inhibition and cellular penetration (Table 1 and Fig. 1), an indication that smaller anthracenediones, such as M2, may access their target, in nuclear DNA, more readily. Cellular and nuclear accessibility is, most likely, a requirement for subsequent anthracenedione-induced DNA damage. Indeed, the second and tightest association of variation in anthracenedione-induced growth inhibition was with the generation of DNA damage, a feature that prompted subsequent investigations into the nature of the drug-induced DNA lesion(s).

4.1. Anthracenedione-induced DNA damage is not mediated via the generation of ROS

A recent report [39] observed that mitoxantrone-induced DNA damage was partially attenuated by the ROS scavenger NAC and logically concluded that ROS were involved in the generation of DNA damage by mitoxantrone. Although the drug can be used as a substrate for the production of ROS via enzymatic reduction of the anthracenedione chromophore [38], it does not readily engage in the pathway [44] since the negative reduction potential of mitoxantrone restricts the metabolic reduction of its chromophore [45], a feature reflected by the absence of any attenuation in anthracenedione-induced DNA damage by NAC (Fig. 4A). It is also noteworthy that all 5,8-dihydroxy-anthracenediones in the present study (Table 1) shared the same chromophore structure yet exhibited a vast spectrum in genotoxic properties (Fig. 2E), further evidence that implicates a mechanism independent of ROS-mediated DNA damage through redox cycling of the chromophore.

4.2. Variation in anthracenedione-induced DNA damage is most likely attributable to a differential ability to stabilise the TOP2 cleavage complex

In contrast to NAC, the TOP2 inhibitor suramin significantly attenuated anthracenedione-induced DNA damage induction (Fig. 4B), implicating the involvement of TOP2 in mediating DNA damage. Suramin is polyanionic in nature and does not detectably bind to DNA [40], and therefore is unlikely to impair a direct anthracenedione–DNA interaction. Evidence suggests suramin directly binds TOP2, itself a basic protein, via electrostatic interactions [40]. Presumably, suramin antagonises anthracenedione-induced DNA damage through sequestration of TOP2 from DNA.

The involvement of TOP2 was independently confirmed through the application of TOP2-compromised HL-60/MX2 cells, which consistently demonstrated a clear resistance to anthracenedione-induced DNA damage, the phosphorylation of H2AX at Ser^{139} and subsequent apoptosis (Figs. 5 and 6). Histone H2AX, a variant member of the nucleosome core, is extensively phosphorylated following DNA damage to generate γH2AX [32,46]. Although there are circumstances where it can represent other DNA lesions, γH2AX induction, specifically γH2AX foci formation,

is widely used as an indirect, yet sensitive marker of DNA DSBs [42,46]. The induction of these γH2AX foci by anthracenediones (Fig. 6) provides a strong indication that these compounds differentially induce DNA damage in the form of DSBs through a TOP2-mediated mechanism and that side-chain composition is a chief determinant in their execution of this mechanism. Most likely, the identity of the primary lesion is an anthracenedione-stabilised TOP2 cleavage complex [47].

4.3. Strict structural requirements exist for efficient TOP2 cleavage complex stabilisation

The parent compound mitoxantrone and its biologically inactive analogue M5 provide crucial clues to the side-chain structural features required for efficient TOP2 stabilisation. Although both compounds contain an identical number of atoms in each side-chain, they demonstrate extreme and opposing genotoxic and growth inhibitory (Table 1) properties, suggesting that side-chain composition, rather than length *per se*, is a chief determinant for activity. Activity was maximal when a basic nitrogen-containing moiety was separated from the anthracenedione chromophore by two methylene units, as in M2, mitoxantrone and pixantrone (Fig. 2F and Table 1). Extension of the primary terminal amino function in M2 through the insertion of successive methylene units, as in M3, M4 and M5, rendered the compound increasingly inactive in terms of growth inhibition (Table 1), DNA damage (Figs. 2, 3, 5–7) and TOP2 catalytic inhibition (Fig. 4C), which was applied as a surrogate indicator of anthracenedione-induced stabilisation of the cleavage complex. Collectively, the pattern strongly suggests that the differential induction of TOP2-mediated DNA damage is dependent on efficient TOP2 cleavage complex stabilisation, and that the position of the side-chain amino group is a crucial determinant of this feature.

The molecular structure of a drug-induced TOP2 cleavage complex has not yet been resolved, however an interfacial model has been proposed where an intercalating drug is situated precisely at the TOP2 cleavage site in a drug–DNA–protein ternary complex [47,48]. In the model, the drug itself comprises two components: first, a DNA-interacting planar chromophore and second, its side-chains, which most likely interact with the enzyme [25,48]. Although highly speculative, it is not difficult to imagine that the relative position of the amino group, as determined by anthracenedione side-chain composition, may be crucial in providing sites of hydrogen bonding or basic sites for interaction with TOP2 catalytic residues.

4.4. ATM is the lead candidate for a role in mediating the anthracenedione-induced DDR

γH2AX is pivotal in mediating numerous signalling pathways in response to DSBs and may achieve this by operating as a recruitment centre for DDR proteins [27,42]. The induction of γH2AX by the anthracenediones, most notably by M2, M3 and mitoxantrone (Figs. 3, 5 and 6), strongly implicates the involvement of at least one protein kinase. The most likely candidates, ATM and ATR, assume the role of chief regulators of the DDR [27] and are responsible for co-ordinating the phosphorylation of many protein substrates, including H2AX. ATM is perhaps the lead candidate in mediating an immediate DNA damage response since the kinase is recognised as a rapid respondent to DSBs (minutes to hours) by phosphorylating H2AX and other protein targets [49], characteristics that are consistent with the anthracenedione-induced damage response (Fig. 7). Moreover, M2-induced Chk2 activation through phosphorylation at Thr^{68} (Fig. 7D) highlights the potential involvement of ATM, the kinase predominantly responsible for Thr^{68} Chk2 phosphorylation [50].

There are also indications that ATR may be involved in mediating an anthracenedione-induced DDR. First, cells replicating their DNA in S phase were most susceptible to M2 and mitoxantrone-induced DNA damage (Fig. 3). ATR-mediated phosphorylation of H2AX is closely coupled with replication-associated stress and DNA damage [51,52]. Second, Chk1 was strongly activated by M2 through Ser^{345} phosphorylation, a potential marker of ATR involvement [50,53], however Chk1 activation was delayed relative to Thr^{68} Chk2 phosphorylation (Fig. 7C and D). The relative delay may indicate an ATM-dependent recruitment of ATR to DSB sites and subsequent phosphorylation of Chk1 [53,54]. Studies have been initiated to identify the relative involvement of ATM and ATR in mediating the initial anthracenedione-induced DDR.

4.5. Potential therapeutic implications for the anthracenedione family of compounds

The chemotherapeutic application of TOP2 poisons is often tempered by their deleterious toxicities [55], a disadvantage that can be potentially overcome through the rational selection and co-administration of compounds that enhance their activity. Unlike its parent mitoxantrone, M5 demonstrates exceptionally low genotoxicity (Figs. 2, 3, 5–7), a high tolerated dose within murine xenograft models (unpublished observations) and may therefore be considered a deactivated TOP2 poison that is non-toxic. Since Mansour et al. [20] have clearly established that M5 generates a highly lethal, ultra-stable DNA adduct following formaldehyde activation, M5 is an excellent candidate for co-administration with formaldehyde-releasing prodrugs. Coupled with the selective targeting of these prodrugs to cancer cells, co-administration with M5 may enable the specific activation of the lethal lesion within cancer cells while avoiding the systemic toxicities typically associated with TOP2 poisons [55].

4.6. The therapeutic value of M2 can potentially be enhanced through the abrogation of G2/M arrest by UCN-01

Perhaps most importantly, Chk1 and Chk2 activation (Fig. 7) provides an indication that cell cycle checkpoints were initiated following M2 exposure. Chk1 and Chk2 are checkpoint kinases that modulate the activity of their cell cycle machinery protein substrates [26,50] in a complex series of pathways that enable cell cycle arrest and DNA repair. Like many tumours, MDA-MB-231 breast cancer cells harbour a mutant form of p53 [56], and are accordingly compromised selectively at the G1/S transition, the first cell cycle checkpoint [26,50]. Cancer cells of this nature are completely reliant on their remaining two intact checkpoints, intra-S and G2/M, to preserve genomic integrity following DNA damage [26,50], a feature that may render them selectively vulnerable relative to p53-proficient normal cells [26]. Given that both Chk1 and Chk2 are key mediators in regulating S and G2/M checkpoints [57], and that M2 efficiently activates both kinases (Fig. 7), it was rationalised that an inhibitor of either or both kinases may abrogate the protracted M2-induced intra-S phase traverse and G2/M arrest (Fig. 7). Abrogation was achieved through the sequential addition of UCN-01, an established Chk1 inhibitor [26,56], and highlighted by the emergence of a very large fraction of multinucleated cells (Fig. 8). Cells of this morphology are most likely undergoing mitotic catastrophe, a form of cell death generated by premature mitosis, in this case, of cells containing unrepaired DNA damage (Fig. 7) [28,50]. The UCN-01-mediated enhancement in mitotic catastrophe provides further evidence of the involvement of Chk1 in the M2-induced DDR, however the participation of other DDR kinases cannot be precluded at this point. UCN-01 demonstrates inhibitory activity against multiple

kinases, including Chk2 and MK2, albeit at significantly greater IC_{50} concentrations than Chk1 [26,50,56].

The identification of these checkpoint kinases has tangible therapeutic benefits given the very strong synergism demonstrated in combining anthracenediones, particularly M2 and mitoxantrone, with UCN-01 to induce growth inhibition (Table 2). The practical application of combining UCN-01 itself with either M2 or mitoxantrone is less likely to succeed, since UCN-01 binds particularly avidly to blood plasma proteins [50], restricting its clinical utility. Nonetheless, the experimental application of UCN-01 has highlighted that the requirement for characterising the anthracenedione-induced DDR is largely worthwhile. The challenge now is to identify its components and how they function in greater detail. Only then can the application of combining anthracenediones, most notably M2 and mitoxantrone, with the next generation of checkpoint kinase inhibitors currently being developed achieve its full potential.

Acknowledgements

This work was supported by the National Health and Medical Research Council in Project Grant 487333 (S.C. and D.P.) and the Contributing to Australian Scholarship and Science Foundation in Project Grant SM/08/1971 (S.C. and B.E.).

References

[1] Bishop JF. Cancer facts: a concise oncology text. Australia: Harwood Academic; 1999.
[2] DeVita VT, Hellman S, Rosenberg SA. Cancer: principles & practice of oncology. Philadelphia; London: Lippincott Williams & Wilkins; 2001.
[3] Faulds D, Balfour JA, Chrisp P, Langtry HD. Mitoxantrone. A review of its pharmacodynamic and pharmacokinetic properties, and therapeutic potential in the chemotherapy of cancer. Drugs 1991;41:400–49.
[4] Mukherji D, Pettengell R. Pixantrone for the treatment of aggressive non-Hodgkin lymphoma. Expert Opin Pharmacother 2010;11:1915–23.
[5] Hazlehurst LA, Krapcho AP, Hacker MP. Correlation of DNA reactivity and cytotoxicity of a new class of anticancer agents: aza-anthracenediones. Cancer Lett 1995;91:115–24.
[6] De Isabella P, Palumbo M, Sissi C, Capranico G, Carenini N, Menta E, et al. Topoisomerase II DNA cleavage stimulation, DNA binding activity, cytotoxicity, and physico-chemical properties of 2-aza- and 2-aza-oxide-anthracenedione derivatives. Mol Pharmacol 1995;48:30–8.
[7] Kapuscinski J, Darzynkiewicz Z. Relationship between the pharmacological activity of antitumor drugs Ametantrone and mitoxantrone (Novatrone) and their ability to condense nucleic acids. Proc Natl Acad Sci USA 1986;83:6302–6.
[8] Feofanov A, Sharonov S, Fleury F, Kudelina I, Nabiev I. Quantitative confocal spectral imaging analysis of mitoxantrone within living K562 cells: intracellular accumulation and distribution of monomers, aggregates, naphtoquinoxaline metabolite, and drug-target complexes. Biophys J 1997;73:3328–36.
[9] Durr FE, Wallace RE, Citarella RV. Molecular and biochemical pharmacology of mitoxantrone. Cancer Treat Rev 1983;10(Suppl. B):3–11.
[10] Hazlehurst LA, Krapcho AP, Hacker MP. Comparison of aza-anthracenedione-induced DNA damage and cytotoxicity in experimental tumor cells. Biochem Pharmacol 1995;50:1087–94.
[11] Smith PJ, Morgan SA, Fox ME, Watson JV. Mitoxantrone-DNA binding and the induction of topoisomerase II associated DNA damage in multi-drug resistant small cell lung cancer cells. Biochem Pharmacol 1990;40:2069–78.
[12] Zwelling LA, Mayes J, Altschuler E, Satitpunwaycha P, Tritton TR, Hacker MP. Activity of two novel anthracene-9,10-diones against human leukemia cells containing intercalator-sensitive or -resistant forms of topoisomerase II. Biochem Pharmacol 1993;46:265–71.
[13] Skladanowski A, Konopa J. Mitoxantrone and ametantrone induce interstrand cross-links in DNA of tumour cells. Br J Cancer 2000;82:1300–4.
[14] Ellis AL, Randolph JK, Conway BR, Gewirtz DA. Biochemical lesions in DNA associated with the antiproliferative effects of mitoxantrone in the hepatoma cell. Biochem Pharmacol 1990;39:1549–56.
[15] Parker BS, Cullinane C, Phillips DR. Formation of DNA adducts by formaldehyde-activated mitoxantrone. Nucleic Acids Res 1999;27:2918–23.
[16] Evison BJ, Mansour OC, Menta E, Phillips DR, Cutts SM. Pixantrone can be activated by formaldehyde to generate a potent DNA adduct forming agent. Nucleic Acids Res 2007;35:3581–9.
[17] Parker BS, Rephaeli A, Nudelman A, Phillips DR, Cutts SM. Formation of mitoxantrone adducts in human tumor cells: potentiation by AN-9 and DNA methylation. Oncol Res 2004;14:279–90.
[18] Evison BJ, Chiu F, Pezzoni G, Phillips DR, Cutts SM. Formaldehyde-activated Pixantrone is a monofunctional DNA alkylator that binds selectively to CpG and CpA doublets. Mol Pharmacol 2008;74:184–94.
[19] Parker BS, Buley T, Evison BJ, Cutts SM, Neumann GM, Iskander MN, et al. A molecular understanding of mitoxantrone-DNA adduct formation: effect of cytosine methylation and flanking sequences. J Biol Chem 2004;279:18814–23.
[20] Mansour OC, Evison BJ, Sleebs BE, Watson KG, Nudelman A, Rephaeli A, et al. New anthracenedione derivatives with improved biological activity by virtue of stable drug-DNA adduct formation. J Med Chem 2010;53:6851–66.
[21] Hurley LH. DNA and its associated processes as targets for cancer therapy. Nat Rev Cancer 2002;2:188–200.
[22] Durr FE. Biochemical pharmacology and tumor biology of mitoxantrone and ametantrone. In: Lown JW, editor. Anthracycline and anthracenedione-based anticancer agents. Amsterdam, The Netherlands: Elsevier; 1988. p. 163–200.
[23] Murdock KC, Child RG, Fabio PF, Angier RB, Wallace RE, Durr FE, et al. Antitumor agents. 1. 1,4-bis[(aminoalkyl)amino]-9,10-anthracenediones. J Med Chem 1979;22:1024–30.
[24] Zee-Cheng RK, Cheng CC. Antineoplastic agents structure-activity relationship study of bis(substituted aminoalkylamino)anthraquinones. J Med Chem 1978;21:291–4.
[25] Krapcho AP, Petry ME, Getahun Z, Landi Jr JJ, Stallman J, Polsenberg JF, et al. 6,9-bis[(aminoalkyl)amino]benzo[g]isoquinoline-5,10-diones. A novel class of chromophore-modified antitumor anthracene-9,10-diones: synthesis and antitumor evaluations. J Med Chem 1994;37:828–37.
[26] Reinhardt HC, Aslanian AS, Lees JA, Yaffe MB. p53-deficient cells rely on ATM- and ATR-mediated checkpoint signaling through the p38MAPK/MK2 pathway for survival after DNA damage. Cancer Cell 2007;11:175–89.
[27] Jackson SP, Bartek J. The DNA-damage response in human biology and disease. Nature 2009;461:1071–8.
[28] Roninson IB, Broude EV, Chang BD. If not apoptosis, then what? Treatment-induced senescence and mitotic catastrophe in tumor cells. Drug Resist Updat 2001;4:303–13.
[29] Jenkins TC. Optical absorbance and fluorescence techniques for measuring DNA-drug interactions. Methods Mol Biol 1997;90:195–218.
[30] Haldane A, Sullivan DM. DNA topoisomerase II-catalyzed DNA decatenation. Methods Mol Biol 2001;95:13–23.
[31] Swift LP, Rephaeli A, Nudelman A, Phillips DR, Cutts SM. Doxorubicin-DNA adducts induce a non-topoisomerase II-mediated form of cell death. Cancer Res 2006;66:4863–71.
[32] MacPhail SH, Banath JP, Yu TY, Chu EH, Lambur H, Olive PL. Expression of phosphorylated histone H2AX in cultured cell lines following exposure to X-rays. Int J Radiat Biol 2003;79:351–8.
[33] Ugarenko M, Nudelman A, Rephaeli A, Kimura K, Phillips DR, Cutts SM. ABT-737 overcomes Bcl-2 mediated resistance to doxorubicin-DNA adducts. Biochem Pharmacol 2010;79:339–49.
[34] Loveland BE, Johns TG, Mackay IR, Vaillant F, Wang ZX, Hertzog PJ. Validation of the MTT dye assay for enumeration of cells in proliferative and antiproliferative assays. Biochem Int 1992;27:501–10.
[35] Evison BJ, Bilardi RA, Chiu FC, Pezzoni G, Phillips DR, Cutts SM. CpG methylation potentiates pixantrone and doxorubicin-induced DNA damage and is a marker of drug sensitivity. Nucleic Acids Res 2009;37:6355–70.
[36] Chou TC, Talalay P. Quantitative analysis of dose-effect relationships: the combined effects of multiple drugs or enzyme inhibitors. Adv Enzyme Regul 1984;22:27–55.
[37] Smith PJ, Desnoyers R, Blunt N, Giles Y, Patterson LH, Watson JV. Flow cytometric analysis and confocal imaging of anticancer alkylaminoanthraquinones and their N-oxides in intact human cells using 647-nm krypton laser excitation. Cytometry 1997;27:43–53.
[38] Basra J, Wolf CR, Brown JR, Patterson LH. Evidence for human liver mediated free-radical formation by doxorubicin and mitozantrone. Anticancer Drug Des 1985;1:45–52.
[39] Huang X, Kurose A, Tanaka T, Traganos F, Dai W, Darzynkiewicz Z. Activation of ATM and histone H2AX phosphorylation induced by mitoxantrone but not by topotecan is prevented by the antioxidant N-acetyl-L-cysteine. Cancer Biol Ther 2006;5:959–64.
[40] Bojanowski K, Lelievre S, Markovits J, Couprie J, Jacquemin-Sablon A, Larsen AK. Suramin is an inhibitor of DNA topoisomerase II in vitro and in Chinese hamster fibrosarcoma cells. Proc Natl Acad Sci USA 1992;89:3025–9.
[41] Harker WG, Slade DL, Parr RL, Feldhoff PW, Sullivan DM, Holguin MH. Alterations in the topoisomerase II alpha gene, messenger RNA, and subcellular protein distribution as well as reduced expression of the DNA topoisomerase II beta enzyme in a mitoxantrone-resistant HL-60 human leukemia cell line. Cancer Res 1995;55:1707–16.
[42] Bonner WM, Redon CE, Dickey JS, Nakamura AJ, Sedelnikova OA, Solier S, et al. GammaH2AX and cancer. Nat Rev Cancer 2008;8:957–67.
[43] Godard T, Deslandes E, Sichel F, Poul JM, Gauduchon P. Detection of topoisomerase inhibitor-induced DNA strand breaks and apoptosis by the alkaline comet assay. Mutat Res 2002;520:47–56.
[44] Doroshow JH, Davies KJ. Comparative cardiac oxygen radical metabolism by anthracycline antibiotics, mitoxantrone, bisantrene, 4′-(9-acridinylamino)-methanesulfon-m-anisidide, and neocarzinostatin. Biochem Pharmacol 1983;32:2935–9.
[45] Reszka K, Hartley JA, Kolodziejczyk P, Lown JW. Interaction of the peroxidase-derived metabolite of mitoxantrone with nucleic acids. Evidence for covalent binding of 14C-labeled drug. Biochem Pharmacol 1989;38:4253–60.

[46] Lobrich M, Shibata A, Beucher A, Fisher A, Ensminger M, Goodarzi AA, et al. GammaH2AX foci analysis for monitoring DNA double-strand break repair: strengths, limitations and optimization. Cell Cycle 2010;9:662–9.
[47] Nitiss JL. Targeting DNA topoisomerase II in cancer chemotherapy. Nat Rev Cancer 2009;9:338–50.
[48] Capranico G, Binaschi M, Borgnetto ME, Zunino F, Palumbo M. A protein-mediated mechanism for the DNA sequence-specific action of topoisomerase II poisons. Trends Pharmacol Sci 1997;18:323–9.
[49] Burma S, Chen BP, Murphy M, Kurimasa A, Chen DJ. ATM phosphorylates histone H2AX in response to DNA double-strand breaks. J Biol Chem 2001;276:42462–7.
[50] Bucher N, Britten CD. G2 checkpoint abrogation and checkpoint kinase-1 targeting in the treatment of cancer. Br J Cancer 2008;98:523–8.
[51] Cliby WA, Lewis KA, Lilly KK, Kaufmann SH. S phase and G2 arrests induced by topoisomerase I poisons are dependent on ATR kinase function. J Biol Chem 2002;277:1599–606.
[52] Ward IM, Chen J. Histone H2AX is phosphorylated in an ATR-dependent manner in response to replicational stress. J Biol Chem 2001;276: 47759–62.
[53] Jazayeri A, Falck J, Lukas C, Bartek J, Smith GC, Lukas J, et al. ATM- and cell cycle-dependent regulation of ATR in response to DNA double-strand breaks. Nat Cell Biol 2006;8:37–45.
[54] Hurley PJ, Bunz F. ATM and ATR: components of an integrated circuit. Cell Cycle 2007;6:414–7.
[55] Seiter K. Toxicity of the topoisomerase II inhibitors. Expert Opin Drug Saf 2005;4:219–34.
[56] Kohn EA, Ruth ND, Brown MK, Livingstone M, Eastman A. Abrogation of the S phase DNA damage checkpoint results in S phase progression or premature mitosis depending on the concentration of 7-hydroxystaurosporine and the kinetics of Cdc25C activation. J Biol Chem 2002;277:26553–64.
[57] Zhou BB, Elledge SJ. The DNA damage response: putting checkpoints in perspective. Nature 2000;408:433–9.